

# Membrane phononic crystals for high- $Q_m$ mechanical defect modes in piezoelectric aluminum nitride

Anastasiia Ciers,<sup>1,\*</sup> Laurentius Radit Nindito,<sup>1</sup> Alexander Jung,<sup>1</sup> Hannes Pfeifer,<sup>1</sup> Armin Dadgar,<sup>2</sup> André Strittmatter,<sup>2</sup> and Witlef Wieczorek<sup>1,†</sup>

<sup>1</sup>*Department of Microtechnology and Nanoscience (MC2),  
Chalmers University of Technology, SE-412 96 Göteborg, Sweden*

<sup>2</sup>*Institute of Physics, Otto-von-Guericke-University Magdeburg, 39106 Magdeburg, Germany*

Nanomechanical resonators with exceptionally low dissipation are advancing mechanics-based sensors and quantum technologies. The key for these advances is the engineering of localized phononic modes that are well-isolated from the environment, i.e., that exhibit a high mechanical quality factor,  $Q_m$ . Membrane phononic crystals fabricated from strained thin films can realize high- $Q_m$  single or multiple localized phononic defect modes. These defect modes can be efficiently interfaced with out-of-plane light or capacitively coupled to a microwave quantum circuit, enabling readout and control of their motion. When membrane phononic crystals are fabricated from a crystalline film, they could offer built-in functionality. We demonstrate a membrane phononic crystal realized in a strained 90 nm-thin film of aluminum nitride (AlN), which is a crystalline piezoelectric material. We engineer a high- $Q_m$  localized phononic defect mode at 1.8 MHz with a  $Q_m \times f_m$ -product of  $1.5 \times 10^{13}$  Hz at room temperature. In future devices, the built-in piezoelectricity of AlN can be utilized for in-situ tuning of mechanical mode frequencies, defect mode couplings, or acoustic bandgaps, which can be used as building blocks of tunable phononic circuits.

Periodic patterning of a material is a well-established method to engineer its effective properties. Phononic crystals (PnC) are structures with periodic variations in the material's mechanical properties with the goal to engineer the localization or propagation of mechanical excitations. PnCs can display phononic bandgaps, ranges in frequency, in which the propagation of elastic waves is prohibited [1]. By engineering phononic bands, mechanical excitations can be efficiently guided [2–4] or confined [5–7]. Using PnCs to localize mechanical excitations results in phononic modes that exhibit ultra-low mechanical dissipation. This is essential for their use in sensing and quantum technology applications [8], for example, in atomic force microscopy [9], microwave-to-optical transduction [10–12], or as a quantum memory [13].

The use of highly-strained thin films enables realization of high- $Q_m$  mechanical modes in the kHz to MHz regime [14], a frequency range relevant for sensing [9] or transduction [11]. Tensile strain thereby allows storing mechanical energy in lossless tensile energy, a method known as dissipation dilution [15]. Combined engineering of the tensile strain distribution in a thin film and of a PnC shield results in soft-clamped, localized mechanical defect modes with ultra-high quality factors [6, 16, 17]. Membrane-based, i.e., two-dimensional, PnCs allow thereby for efficient interfacing to out-of-plane light [6, 17, 18], coupling to superconducting circuits [18, 19], or realization of coupled defect modes [20]. Such membrane PnC structures have approached quality factors of  $10^9$  at room temperature based on thin strained films of amorphous  $\text{Si}_3\text{N}_4$ , realized through subtractive [6, 16, 21]

or additive density modulation [22, 23]. Although amorphous  $\text{Si}_3\text{N}_4$  is an excellent material for high- $Q_m$  nanomechanics, it lacks functionality. Crystalline films with large tensile strain, however, can offer built-in functionality, such as piezoelectricity or superconductivity, and at the same time realize high- $Q_m$  nanomechanical devices. In particular, piezoelectricity can be used to actively modulate mechanical properties such as mode frequency, phononic bandgap, or coupling between localized phononic modes, which can be utilized in phononic circuits [24]. Furthermore, piezoelectric materials allow realizing optoelectromechanical devices for microwave-to-optics conversion [25, 26]. So far, high- $Q_m$  nanomechanical resonators in the kHz to MHz frequency range have been demonstrated with the piezoelectric materials InGaP [27–29], SiC [30], or AlN [31, 32]. However, the geometry of these devices was restricted to one-dimensional structures, such as uniform [28, 30, 32] or PnC beams [31], or two-dimensional structures such as membrane [27], trampoline [29] or hierarchical resonators [31] that do not exploit a PnC.

In our work, we realize high- $Q_m$  mechanical defect modes in a membrane PnC in tensile-strained 90 nm-thin piezoelectric AlN. We adapt a hexagonal PnC, a so-called dandelion, previously demonstrated with  $\text{Si}_3\text{N}_4$  [21]. Fig. 1(a) shows a unit cell of the hexagonal PnC lattice that we use to pattern the AlN film. A hexagonal PnC realizes a wider bandgap compared to a square-lattice PnC [33, 34] and, thus, isolates a PnC defect mode more effectively [35]. Furthermore, the hexagonal lattice has  $60^\circ$  in-plane rotational symmetry and, thus, follows the crystal structure and, therefore, stress distribution in AlN [32]. This is advantageous as the hexagonal lattice avoids an undesired directional variation of the PnC bandgap.

Fig. 1(b) shows the band structure of the first ir-

\* anastasiia.ciers@chalmers.se

† witlef.wieczorek@chalmers.se

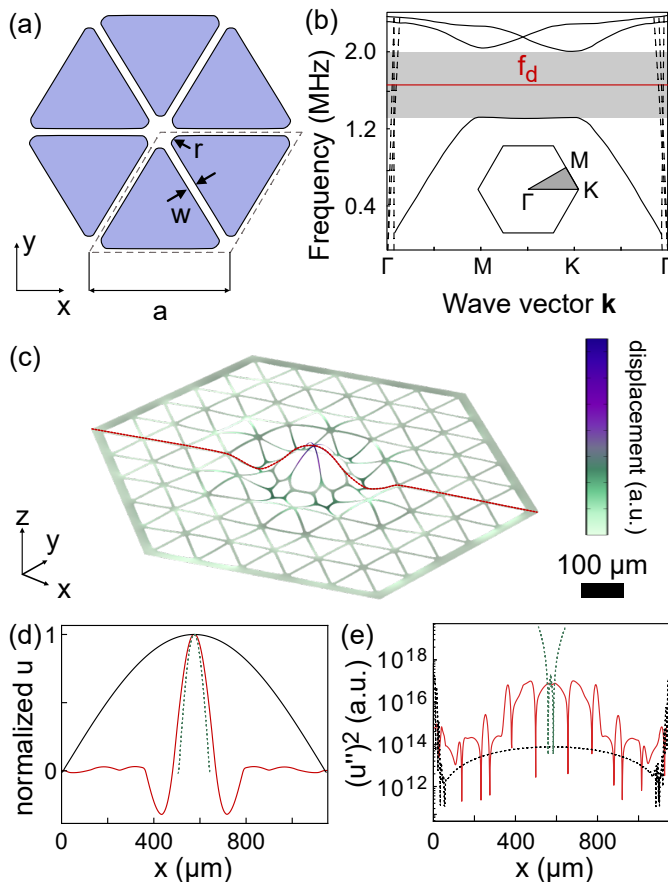


Figure 1. **Simulation of the unit cell and defect mode in a hexagonal PnC.** (a) PnC unit cell with lattice constant  $a$  and triangular holes with fillet radius  $r$  and tether width  $w$ . Dashed lines mark the primitive unit cell. (b) Phononic band structure of the unit cell showing a quasi-bandgap in the gray area. Solid lines are out-of-plane modes and dashed lines are in-plane modes. The red line indicates the defect-mode frequency  $f_d$  for  $d_h = 45 \mu\text{m}$ . (c) Mechanical displacement of the defect mode. (d) The displacement profile,  $u$ , and (e) squared curvature (linked to bending loss) for the defect mode along the red line marked in (c). Dashed lines are a comparison to a uniform beam of the same length (2.2 mm) as the PnC structure (black) and of a  $135 \mu\text{m}$ -long beam with a frequency of 1.6 MHz that is similar to the defect-mode frequency (green).

reducible Brillouin zone of the PnC along the high-symmetry points  $\Gamma$ , M, and K (see the inset Fig. 1(b)). The band structure is obtained from finite element method (FEM) eigenfrequency simulations (details in Appendix). We simulate AlN as an isotropic material with a Young’s modulus of 313 GPa [32]. We obtain a 40% bandgap for out-of-plane modes around 1.66 MHz (Fig. 1(b)) with the chosen pattern of rounded triangular holes defined by the lattice period  $a = 110 \mu\text{m}$ , tether width  $w = 6.4 \mu\text{m}$ , and fillet radius  $r = 5 \mu\text{m}$  (see Fig. 1(a)). Note that a pattern with circular holes would also result in a large bandgap [6]. However, such PnC design does not withstand the isotropic release process

that we use for releasing the AlN layer (see Appendix).

We introduce a defect mode in the PnC by a variation of two unit cells from the center in all directions. The central defect pad has a diameter of  $8.7 \mu\text{m}$  and is supported by  $2.6 \mu\text{m}$ -wide tethers that taper to  $4.5 \mu\text{m}$  and then to  $w = 6.4 \mu\text{m}$  [21]. This results in a stress enhancement at the defect (see Fig. 2(c)), which is beneficial for increasing  $Q_m$ . Similarly to Ref. [21], we patterned additional hexagonal holes of size  $d_h$  in the pads directly adjacent to the central pad (see Fig. 1(c)) leading to a gentler delocalization and, consequently, to a smaller bending of the mode, and also to the possibility to tune the frequency of the defect mode and optimize its quality factor. For example, for  $d_h = 45 \mu\text{m}$  the localized mode has a frequency of 1.64 MHz, i.e., it is placed in the center of the PnC bandgap. Fig. 1(d) shows the displacement profile of this defect mode, which is localized to the defect site, and strongly attenuated towards the clamping points due to the PnC. Fig. 1(d) furthermore compares this displacement profile to the one of a 2.2 mm-long beam, whose length is the same as the total PnC device, and to a  $135 \mu\text{m}$ -long beam, which has the same mechanical frequency as the defect mode of the PnC. We observe that the fundamental mode of the 2.2 mm-long beam lacks the confinement that is achieved by the PnC membrane. Fig. 1(e) shows the bending of the defect mode, which is much smaller at the clamping points compared to the uniform beams. Therefore, such a localized defect mode will exhibit a reduced bending loss.

To analyze the attainable  $Q_m$  of the defect mode, we consider that its total  $Q_m$  can be expressed as a sum of three dominant contributions:

$$\frac{1}{Q_m} = \frac{1}{Q_{\text{gas}}} + \frac{1}{Q_{\text{rad}}} + \frac{1}{Q_D}, \quad (1)$$

where  $Q_{\text{gas}}$  is the gas-limited quality factor (neglected in the following as we measure the devices in ultra-high vacuum),  $Q_{\text{rad}}$  is the quality factor that is limited by radiation loss [36, 37] and  $Q_D$  is the diluted internal quality factor [38]. The latter is given by

$$Q_D = D_Q \times Q_{\text{int}}, \quad (2)$$

where the intrinsic quality factor for 90 nm-thin AlN [32] is  $Q_{\text{int}} = 7.4 \times 10^3$  and  $D_Q$  can be calculated from the ratio of the kinetic to the bending energy [31, 39],  $E_{\text{kin}}$  and  $U_{\text{bend}}$ , which we obtain from FEM simulations of the resonator geometry.

We vary  $d_h$  from 0 (no hole) to  $60 \mu\text{m}$  (Fig. 2(a)) to tune the defect mode’s frequency and analyze the effect on  $Q_D$ . Fig. 2(b) shows that we obtain a non-monotonous behavior. The defect mode’s frequency increases up to  $d_h = 45 \mu\text{m}$  due to shortening of the tethers and an increased stress in the center region, see Fig. 2(c). Above  $d_h = 45 \mu\text{m}$ , the frequency decreases slightly, which we attribute to a small increase in the motional mass of the mode, see Fig. 2(d). To understand the behavior of  $Q_D$ , we notice that the defect-mode frequency is further away

from the mid-bandgap frequency when  $d_h$  is smaller than 25  $\mu\text{m}$ . This results in a weaker localization of the defect mode concomitant with an increase in bending energy (Fig. 2(d)). This results in a lower  $Q_D$  compared to the high  $Q_D$  achieved with  $d_h$  between 30  $\mu\text{m}$  and 55  $\mu\text{m}$ . For  $d_h$  of 60  $\mu\text{m}$  we observe a strong increase in the bending energy (Fig. 2(d)), which explains the observed reduction in  $Q_D$ .

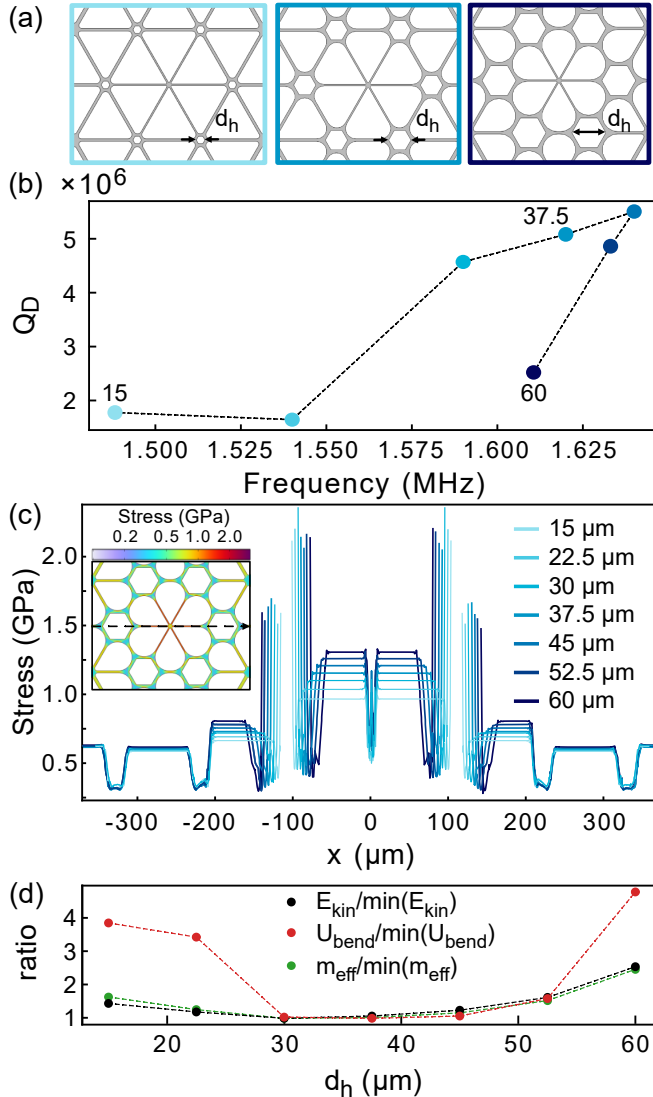


Figure 2. **FEM simulations for the PnC defect mode with different defect sites.** (a) Schematics of defect sites with  $d_h = 15$   $\mu\text{m}$ , 37.5  $\mu\text{m}$ , and 60  $\mu\text{m}$ . (b)  $Q_D$  vs. frequency of the defect mode for different  $d_h$ . (c) Stress along the tethers of the defect site and PnC (dashed line in inset) for different  $d_h$ . The inset shows the stress distribution for the defect site with  $d_h = 60$   $\mu\text{m}$ . (d) The hole size  $d_h$  influences the kinetic energy (black), bending energy (red), and the motional mass (green) of the localized defect mode.

To evaluate a potential limitation of  $Q_m$  by the radiation-limited quality factor  $Q_{\text{rad}}$ , we analyze radiation loss. To this end, we vary the number of unit cells

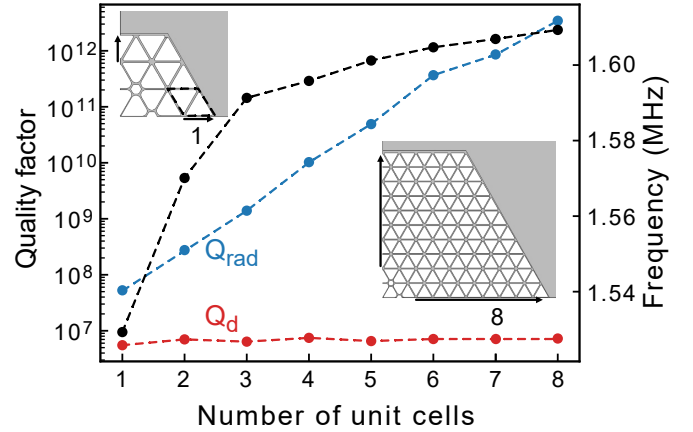


Figure 3. **Membrane PnC defect mode properties versus unit cell number.** Dissipation-diluted quality factor  $Q_D$  (red), radiation-limited quality factor  $Q_{\text{rad}}$  (blue), and defect-mode frequency  $f_d$  (black) obtained from FEM simulations.

around the defect site from 1 to 8 and evaluate loss of mechanical energy to the substrate via FEM simulations (see Appendix). Fig. 3 shows that  $Q_{\text{rad}}$  increases exponentially with the number of unit cells, which demonstrates efficient shielding, while  $Q_D$  remains approximately constant. Furthermore, we observe a slight increase in the defect-mode frequency, which we attribute to a stronger localization of the mode with an increase in the number of unit cells. Therefore, for our experiments, we choose to fabricate PnC devices with three rows of unit cells, which guarantees that these devices are not limited by  $Q_{\text{rad}}$ . Furthermore, we select the PnC structures with  $d_h = (37.5, 45, 52.5)$   $\mu\text{m}$  as their defect mode frequency  $f_d$  is closest to the mid-bandgap frequency resulting in the highest values of  $Q_D$  (see Fig. 2(b)).

We fabricate membrane PnC devices from an AlN film with a thickness of 90 nm that is grown by metal-organic vapor-phase epitaxy (MOVPE) directly on a Si (111) substrate. This yields a crystalline film with residual stress of 790 MPa [32], for details on the film quality see Ref. [32]. We use electron-beam lithography and a subsequent  $\text{XeF}_2$ -based release process for fabrication of the membrane PnCs, for details see Ref. [31]. Fig. 4(a) shows a scanning electron microscope (SEM) image of a fabricated 90 nm-thin PnC device and Fig. 4(b) shows the defect site in the PnC. We characterize the mechanical properties of the devices using an interferometric displacement measurement setup, where the samples are placed in ultra-high vacuum ( $4.6 \times 10^{-8}$  mbar) at room temperature [31, 32]. Fig. 4(c) shows the noise power spectrum (NPS) of a PnC device with  $d_h = 45$   $\mu\text{m}$ . We observe a clear and well-isolated signal of the defect mode at a frequency of 1.83 MHz. Fig. 4(d) shows a ring-down measurement of this mode, from which we obtain a  $Q_m$  of  $8.2 \times 10^6$ , yielding a  $Q_m \times f_m$ -product of  $1.5 \times 10^{13}$  Hz. The calculated force sensitivity for this defect mode using

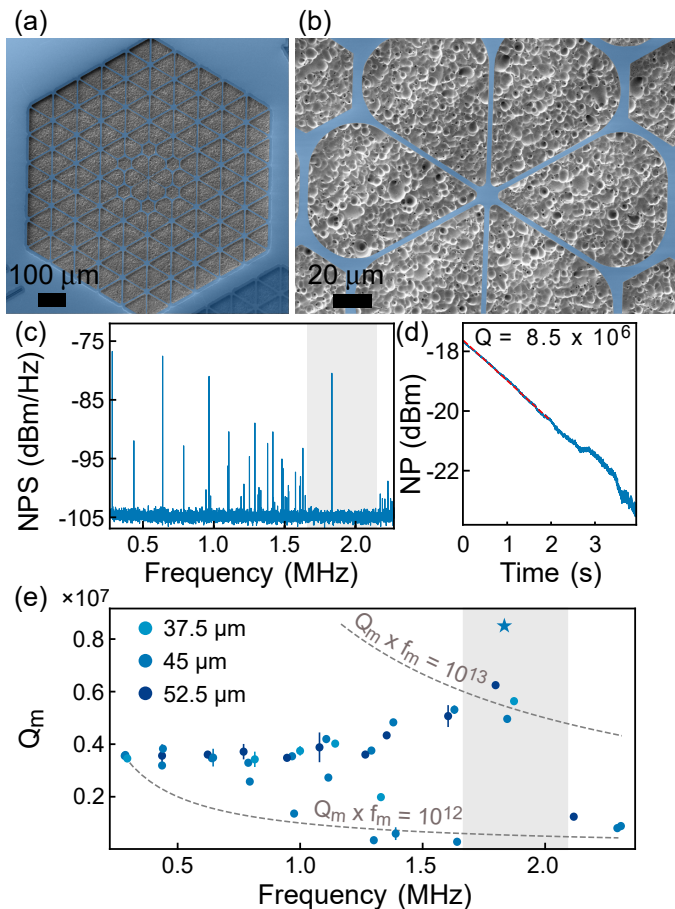


Figure 4. **Measurements of AlN dandelion membrane PnCs.** (a) False-colored SEM image of a released PnC device. (b) A close-up SEM image of the defect-site. (c) NPS of the membrane PnC with  $d_h = 45 \mu\text{m}$ . Gray area highlights the observed quasi-bandgap. (d) Ring-down measurement of the localized defect mode marked as a star in (e). (e) Measured frequencies and corresponding  $Q_m$  of non-localized and defect modes observed from four PnC devices with  $d_h = (37.5, 45, 52.5)\mu\text{m}$ .

a simulated motional mass of  $0.4 \text{ ng}$  at room temperature is  $99 \text{ aN}/\sqrt{\text{Hz}}$ , similar to Ref. [16] ( $104 \text{ aN}/\sqrt{\text{Hz}}$ ) and a factor of two larger than Ref. [6] ( $55 \text{ aN}/\sqrt{\text{Hz}}$ ).

| $d_h$ ( $\mu\text{m}$ ) | $f_d^{\text{FEM}}$ (MHz) | $f_d^{\text{meas}}$ (MHz) | $Q_D^{\text{FEM}}$ | $Q_m^{\text{meas}}$ |
|-------------------------|--------------------------|---------------------------|--------------------|---------------------|
| 37.5                    | 1.62                     | 1.87                      | $5.1 \times 10^6$  | $5.6 \times 10^6$   |
| 45                      | 1.64                     | 1.83                      | $5.5 \times 10^6$  | $8.2 \times 10^6$   |
| 52.5                    | 1.63                     | 1.79                      | $4.9 \times 10^6$  | $6.2 \times 10^6$   |

Table I. Simulated and measured values for the localized defect mode. Parameters:  $a = 110 \mu\text{m}$ ,  $r = 5 \mu\text{m}$ .

Fig. 4(e) summarizes the measured quality factors  $Q_m$  for the localized defect modes and non-localized modes of four fabricated devices. The largest quality factors and  $Q_m \times f_m$ -products are observed for the localized de-

fect modes, as expected. Tab. I compares simulated and measured values for three defect-site geometries with different  $d_h$ . We obtain a reasonable agreement between simulated  $Q_D$  and measured  $Q_m$ . This agreement supports that the fabricated membrane PnC structures in AlN are indeed limited by dissipation dilution. However, we find that the FEM simulations underestimate the defect mode frequency by 10%. This discrepancy could be due to a higher stress in the film compared to the value used for the FEM simulations or a small remaining in-plane stress anisotropy of the AlN crystalline film [32].

To conclude, we have realized dandelion [21] membrane phononic crystals in a crystalline  $90 \text{ nm}$ -thin film of piezoelectric AlN. The membrane PnC supported a localized mechanical mode, where the best device reached a mechanical quality factor of  $8.2 \times 10^6$  exploiting dissipation dilution via strain in the thin film and soft clamping via localization of the defect mode in the PnC. The  $Q_m \times f_m$ -product of  $1.5 \times 10^{13} \text{ Hz}$  supports a coherent mechanical oscillation at room temperature. Higher quality factors could be realized by improving the material quality or further engineering of the device geometry. By using thinner AlN films, higher dilution factors can be achieved provided that the strain and intrinsic quality factor of the film remain large. The membrane PnC device geometry can be further engineered by optimizing the PnC patterning [40], by exploiting strain engineering [41], e.g. through further tapering of the tethers, or by exploring additive density modulation instead of etching holes [22, 23]. Membrane PnCs realized with AlN could make use of the built-in piezoelectricity in hybrid high- $Q_m$  optoelectromechanical devices for in-situ tunable phononic circuits [24], topological phononics [42], or microwave-to-optics conversion [10, 18, 26, 43].

## ACKNOWLEDGMENTS

We thank Joachim Ciers for valuable discussions and support with ellipsometry measurements. This work was supported by the Knut and Alice Wallenberg (KAW) Foundation through a Wallenberg Academy Fellowship (W.W.), the KAW project no. 2022.0090, and the Wallenberg Center for Quantum Technology (WACQT, A.C.). H.P. acknowledges funding by the European Union under the project MSCA-PF-2022-OCOMM. MOVPE of AlN on Si was performed at Otto-von-Guericke-University Magdeburg. The mechanical resonators were fabricated in the Myfab Nanofabrication Laboratory at Chalmers.

## DATA AVAILABILITY

Data underlying the results presented in this paper are available in the open-access Zenodo database: <https://doi.org/10.5281/zenodo.14778128> [44].

- 
- [1] M. Maldovan, Sound and heat revolutions in phononics, *Nature* **503**, 209 (2013).
- [2] H. Pfeifer, T. Paraiso, L. Zang, and O. Painter, Design of tunable GHz-frequency optomechanical crystal resonators, *Optics express* **24**, 11407 (2016).
- [3] M. Ghasemi Baboly, C. M. Reinke, B. A. Griffin, I. El-Kady, and Z. Leseman, Acoustic waveguiding in a silicon carbide phononic crystals at microwave frequencies, *Applied Physics Letters* **112**, 10.1063/1.5016380 (2018).
- [4] X. Xi, I. Chernobrovkin, J. Kořata, M. B. Kristensen, E. C. Langman, A. S. Sørensen, O. Zilberberg, and A. Schliesser, A soft-clamped topological waveguide for phonons, arXiv preprint arXiv:2408.08717 10.48550/arXiv.2408.08717 (2024).
- [5] P.-L. Yu, K. Cicak, N. Kampel, Y. Tsaturyan, T. Purdy, R. Simmonds, and C. Regal, A phononic bandgap shield for high-q membrane microresonators, *Applied Physics Letters* **104**, 023510 (2014).
- [6] Y. Tsaturyan, A. Barg, E. S. Polzik, and A. Schliesser, Ultracoherent nanomechanical resonators via soft clamping and dissipation dilution, *Nature Nanotechnology* **12**, 776 (2017).
- [7] M. Eichenfield, J. Chan, R. M. Camacho, K. J. Vahala, and O. Painter, Optomechanical crystals, *Nature* **462**, 78 (2009).
- [8] S. Barzanjeh, A. Xuereb, S. Gröblacher, M. Paternostro, C. A. Regal, and E. M. Weig, Optomechanics for quantum technologies, *Nature Physics* **18**, 15 (2022).
- [9] D. Hälg, T. Gisler, Y. Tsaturyan, L. Catalini, U. Grob, M.-D. Krass, M. Hérítier, H. Mattiat, A.-K. Thamm, R. Schirhagl, *et al.*, Membrane-based scanning force microscopy, *Physical Review Applied* **15**, L021001 (2021).
- [10] M. Mirhosseini, A. Sipahigil, M. Kalaei, and O. Painter, Superconducting qubit to optical photon transduction, *Nature* **588**, 599 (2020).
- [11] R. Delaney, M. Urmeý, S. Mittal, B. Brubaker, J. Kindem, P. Burns, C. Regal, and K. Lehnert, Superconducting-qubit readout via low-backaction electro-optic transduction, *Nature* **606**, 489 (2022).
- [12] W. Jiang, F. M. Mayor, S. Malik, R. Van Laer, T. P. McKenna, R. N. Patel, J. D. Witmer, and A. H. Safavi-Naeini, Optically heralded microwave photon addition, *Nature Physics* **19**, 1423 (2023).
- [13] A. Wallucks, I. Marinković, B. Hensen, R. Stockill, and S. Gröblacher, A quantum memory at telecom wavelengths, *Nature Physics* **16**, 772 (2020).
- [14] N. J. Engelsen, A. Beccari, and T. J. Kippenberg, Ultrahigh-quality-factor micro-and nanomechanical resonators using dissipation dilution, *Nature Nanotechnology*, 1 (2024).
- [15] S. A. Fedorov, N. J. Engelsen, A. H. Ghadimi, M. J. Beryhi, R. Schilling, D. J. Wilson, and T. J. Kippenberg, Generalized dissipation dilution in strained mechanical resonators, *Physical Review B* **99**, 054107 (2019).
- [16] C. Reetz, R. Fischer, G. G. Assumpcao, D. P. McNally, P. S. Burns, J. C. Sankey, and C. A. Regal, Analysis of membrane phononic crystals with wide band gaps and low-mass defects, *Physical Review Applied* **12**, 044027 (2019).
- [17] T. J. Clark, S. Bernard, J. Ma, V. Dumont, and J. C. Sankey, Optically defined phononic crystal defect, *Physical Review Letters* **133**, 226904 (2024).
- [18] B. M. Brubaker, J. M. Kindem, M. D. Urmeý, S. Mittal, R. D. Delaney, P. S. Burns, M. R. Vissers, K. W. Lehnert, and C. A. Regal, Optomechanical ground-state cooling in a continuous and efficient electro-optic transducer, *Physical Review X* **12**, 021062 (2022).
- [19] Y. Seis, T. Capelle, E. Langman, S. Saarinen, E. Planz, and A. Schliesser, Ground state cooling of an ultracoherent electromechanical system, *Nature communications* **13**, 1507 (2022).
- [20] L. Catalini, Y. Tsaturyan, and A. Schliesser, Soft-clamped phononic dimers for mechanical sensing and transduction, *Physical Review Applied* **14**, 014041 (2020).
- [21] S. A. Saarinen, N. Kralj, E. C. Langman, Y. Tsaturyan, and A. Schliesser, Laser cooling a membrane-in-the-middle system close to the quantum ground state from room temperature, *Optica* **10**, 364 (2023).
- [22] D. Høj, U. B. Hoff, and U. L. Andersen, Ultracoherent nanomechanical resonators based on density phononic crystal engineering, *Physical Review X* **14**, 011039 (2024).
- [23] G. Huang, A. Beccari, N. J. Engelsen, and T. J. Kippenberg, Room-temperature quantum optomechanics using an ultralow noise cavity, *Nature* **626**, 512 (2024).
- [24] J. C. Taylor, E. Chatterjee, W. F. Kindel, D. Soh, and M. Eichenfield, Reconfigurable quantum phononic circuits via piezo-acoustomechanical interactions, *npj Quantum Information* **8**, 19 (2022).
- [25] A. Vainsencher, K. Satzinger, G. Peairs, and A. Cleland, Bi-directional conversion between microwave and optical frequencies in a piezoelectric optomechanical device, *Applied Physics Letters* **109**, 033107 (2016).
- [26] W. Jiang, C. J. Sarabalis, Y. D. Dahmani, R. N. Patel, F. M. Mayor, T. P. McKenna, R. Van Laer, and A. H. Safavi-Naeini, Efficient bidirectional piezo-optomechanical transduction between microwave and optical frequency, *Nature communications* **11**, 1166 (2020).
- [27] G. D. Cole, P.-L. Yu, C. Gärtner, K. Siquans, R. Moghadas Nia, J. Schmöle, J. Hoelscher-Obermaier, T. P. Purdy, W. Wiczorek, C. A. Regal, and M. Aspelmeyer, Tensile-strained  $\text{In}_x\text{Ga}_{1-x}\text{P}$  membranes for cavity optomechanics, *Applied Physics Letters* **104**, 201908 (2014).
- [28] M. Bückle, V. C. Hauber, G. D. Cole, C. Gärtner, U. Zeimer, J. Grenzer, and E. M. Weig, Stress control of tensile-strained  $\text{In}_x\text{Ga}_{1-x}\text{P}$  nanomechanical string resonators, *Applied Physics Letters* **113**, 201903 (2018).
- [29] S. K. Manjeshwar, A. Ciers, F. Hellman, J. Blasing, A. Strittmatter, and W. Wiczorek, High-Q trampoline resonators from strained crystalline  $\text{InGaP}$  for integrated free-space optomechanics, *Nano Letters* **23**, 5076 (2023).
- [30] L. Sementilli, D. M. Lukin, H. Lee, E. Romero, J. Vučković, and W. P. Bowen, Ultralow dissipation nanomechanical devices from monocrystalline silicon carbide, arXiv preprint arXiv:2404.13893 10.48550/arXiv.2404.13893 (2024).
- [31] A. Ciers, A. Jung, J. Ciers, L. R. Nindito, H. Pfeifer, A. Dadgar, A. Strittmatter, and W. Wiczorek, Nanomechanical crystalline  $\text{AlN}$  resonators with high quality factors for quantum optoelectromechanics, *Advanced Mate-*

- rials **36**, 2403155 (2024).
- [32] A. Ciers, A. Jung, J. Ciers, L. R. Nindito, H. Pfeifer, A. Dadgar, J. Bläsing, A. Strittmatter, and W. Wiczorek, Thickness dependence of the mechanical properties of piezoelectric high-Qm nanomechanical resonators made from aluminium nitride, *Materials for Quantum Technology* **4**, 046301 (2024).
- [33] M. Kushwaha and P. Halevi, Giant acoustic stop bands in two-dimensional periodic arrays of liquid cylinders, *Applied Physics Letters* **69**, 31 (1996).
- [34] W. Kuang, Z. Hou, and Y. Liu, The effects of shapes and symmetries of scatterers on the phononic band gap in 2D phononic crystals, *Physics Letters A* **332**, 481 (2004).
- [35] P. Wang, Y. Zheng, M. C. Fernandes, Y. Sun, K. Xu, S. Sun, S. H. Kang, V. Tournat, and K. Bertoldi, Harnessing geometric frustration to form band gaps in acoustic channel lattices, *Physical Review Letters* **118**, 084302 (2017).
- [36] G. D. Cole, I. Wilson-Rae, K. Werbach, M. R. Vanner, and M. Aspelmeyer, Phonon-tunnelling dissipation in mechanical resonators, *Nature Communications* **2**, 231 (2011).
- [37] M. H. de Jong, M. A. ten Wolde, A. Cupertino, S. Gröblacher, P. G. Steeneken, and R. A. Norte, Mechanical dissipation by substrate-mode coupling in sin resonators, *Applied Physics Letters* **121**, 032201 (2022).
- [38] G. I. Gonzfilez and P. R. Saulson, Brownian motion of a mass suspended by an anelastic wire, *Journal of the Acoustical Society of America* **96**, 207 (1994).
- [39] Q. P. Unterreithmeier, T. Faust, and J. P. Kotthaus, Damping of nanomechanical resonators, *Physical Review Letters* **105**, 027205 (2010).
- [40] Z. Zhang, Y. F. Li, F. Meng, and X. Huang, Topological design of phononic band gap crystals with sixfold symmetric hexagonal lattice, *Computational Materials Science* **139**, 97 (2017).
- [41] A. H. Ghadimi, S. A. Fedorov, N. J. Engelsen, M. J. Breyhi, R. Schilling, D. J. Wilson, and T. J. Kippenberg, Elastic strain engineering for ultralow mechanical dissipation, *Science* **360**, 764 (2018).
- [42] T. Vasileiadis, J. Varghese, V. Babacic, J. Gomis-Bresco, D. Navarro Urrios, and B. Graczykowski, Progress and perspectives on phononic crystals, *Journal of Applied Physics* **129**, 160901 (2021).
- [43] M. J. Weaver, P. Duivesteyn, A. C. Bernasconi, S. Scharmer, M. Lemang, T. C. v. Thiel, F. Hijazi, B. Hensen, S. Gröblacher, and R. Stockill, An integrated microwave-to-optics interface for scalable quantum computing, *Nature Nanotechnology* **19**, 166 (2024).
- [44] A. Ciers, L. R. Nindito, A. Jung, H. Pfeifer, A. Dadgar, A. Strittmatter, and W. Wiczorek, Membrane phononic crystals for high-q.m mechanical defect modes in piezoelectric aluminum nitride, [10.5281/zenodo.14778128](https://arxiv.org/abs/10.5281/zenodo.14778128) (2025).
- [45] D. Mason, J. Chen, M. Rossi, Y. Tsaturyan, and A. Schliesser, Continuous force and displacement measurement below the standard quantum limit, *Nature Physics* **15**, 745 (2019).

## Appendix A: Supplementary material

### 1. Fabrication

Fig. 5 shows an optical image of a successfully fabricated dandelion [21] membrane PnC in 90 nm-thin AlN.

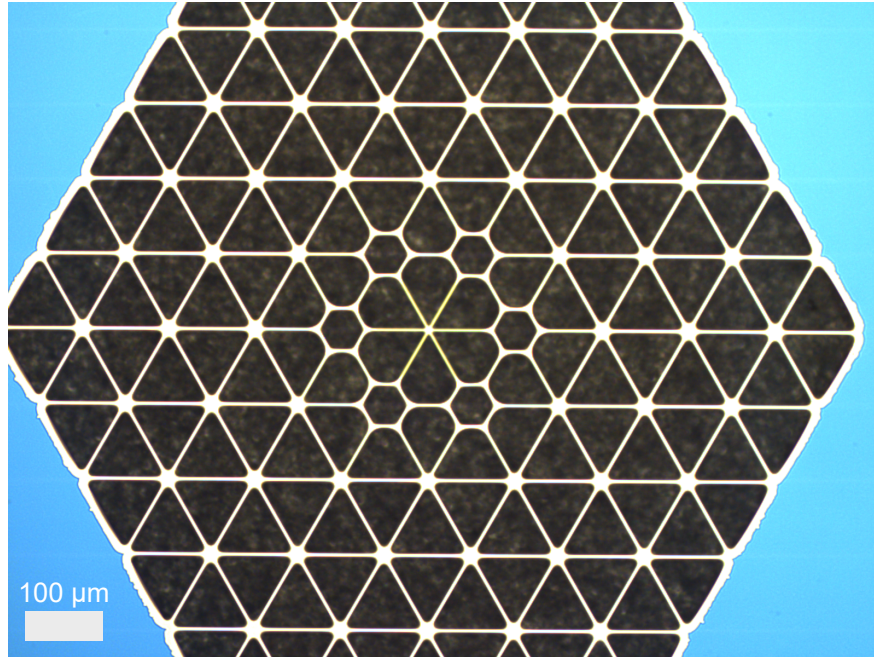


Figure 5. **Optical image of a dandelion membrane PnC with rounded triangular holes.**  $d_h = 37.5 \mu\text{m}$ .

### 2. Simulations

#### a. Parameters

For all FEM simulations we start by performing a stationary solution to evaluate the redistributed stress in the PnC. Then we simulate the eigenfrequencies of the mechanical modes. The parameters used in the FEM simulation are given in Tab. II. For bandstructure simulations Bloch-Floquet periodicity is imposed on the boundaries along the in-plane directions, and the wave vector  $k$  is swept across the first Brillouin zone.

| Symbol                     | Description              | Value             | Unit              |
|----------------------------|--------------------------|-------------------|-------------------|
| $\rho$                     | density                  | 3255              | kg/m <sup>3</sup> |
| $\nu$                      | Poisson's ratio          | 0.287             |                   |
| $h$                        | layer thickness          | 90                | nm                |
| $\sigma_{\text{residual}}$ | as-grown stress          | 0.79              | GPa               |
| $E$                        | Young's modulus          | 313               | GPa               |
| $Q_{\text{int}}$           | intrinsic quality factor | $7.4 \times 10^3$ |                   |

Table II. FEM simulation parameters of the 90 nm-thin AlN film [32].

b. Force sensitivity

The motional mass  $m_{\text{eff}}$  is evaluated with respect to a point-like laser probe centered on the maximum of the displacement field:

$$m_{\text{eff}} = \frac{\rho \iint u^2 dx dy}{\max(u^2)}. \quad (\text{A1})$$

For the distributed modes  $m_{\text{eff}}$  is between 1 and 10 ng, while the localized mode is below 1 ng, e.g.  $m_{\text{eff}} = 0.43$  ng for  $d_h = 45$   $\mu\text{m}$ . The motional mass was used to calculate the force sensitivity  $S_F = \sqrt{4k_B T m_{\text{eff}} \Gamma_m}$  for the defect modes, see Tab. III.

| $d_h$ ( $\mu\text{m}$ ) | $m_{\text{eff}}$ (ng) | $f_d^{\text{meas}}$ (MHz) | $Q_m^{\text{meas}}$ | $\sqrt{S_F}$ (aN/ $\sqrt{\text{Hz}}$ ) |
|-------------------------|-----------------------|---------------------------|---------------------|--|
| 37.5                    | 0.37                  | 1.87                      | $5.6 \times 10^6$   | 114                                    |
| 45                      | 0.43                  | 1.83                      | $8.2 \times 10^6$   | 99.4                                   |
| 52.5                    | 0.56                  | 1.79                      | $6.2 \times 10^6$   | 129.7                                  |

Table III. FEM values of  $m_{\text{eff}}$  in dependence on  $d_h$  ( $a = 110$   $\mu\text{m}$ ,  $r = 5$   $\mu\text{m}$ ). The FEM simulation values were obtained with the parameters from Tab. II.

c. Radiation loss

To evaluate the radiation loss  $Q_{\text{rad}}$ , we use the complex eigenfrequency obtained from FEM simulations [37]:

$$Q_{\text{rad}} = \frac{\text{Re}[f_d]}{2\text{Im}[f_d]}. \quad (\text{A2})$$

The magnitude of radiation loss is dependent on both the impedance and mode matching between the resonator and substrate, as well as the geometry of the resonator, and how the sample is mounted for the measurements. To reduce the interference of reflected waves, the outer boundaries are defined as perfectly matched layers (PML). The evaluation of the radiation loss drastically depends on the setting of the PML. The speed of the acoustic wave in AlN is  $v = 11$  km/s and in Si  $v = 8.4$  km/s. Then, the wavelength for a frequency of  $f_m = 1.5$  MHz is given as  $\lambda = v/f_m$ , yielding  $\lambda_{\text{AlN}} = 7.33$  mm and  $\lambda_{\text{Si}} = 5.6$  mm. The PML should be somewhere between half and quarter of this wavelength (1.83 to 3.67 mm) in order to attenuate the wave to a negligible amplitude before it reaches the outer boundary of the PML, while being short enough to keep computational costs reasonable. We set the PML to 3 mm and simulated a quarter of the actual structure (exploiting mirror symmetry). We introduce an additional transition layer (TL) of material between the clamping point of the PnC and the PML to avoid an abrupt change in material properties and therefore numerical artifacts. An empirical choice of the TL is about one eighth of the acoustic wavelength. Fig. 6(a,b) shows the displacement obtained from such FEM simulations for the localized high- $Q_{\text{rad}}$  defect mode and a non-localized low- $Q_{\text{rad}}$  mode.

### 3. PnC with circular holes

Inspired by Refs. [6, 45], we adapt a honeycomb PnC geometry for realizing a PnC in the AlN thin film. Fig. 7(a) shows a primitive unit cell of the hexagonal lattice with lattice constant  $a$  and circular holes of radius  $r$ .

| Hole type | $a$ ( $\mu\text{m}$ ) | $r$ ( $\mu\text{m}$ ) | $f_d^{\text{FEM}}$ (MHz) | $Q_m^{\text{FEM}}$ |
|-----------|-----------------------|-----------------------|--------------------------|--------------------|
| Round     | 110                   | 0.245a                | 1.87                     | $7.1 \times 10^6$  |

Table IV. Honeycomb PnC membrane simulation parameters and results.

For the parameters taken from Tab. IV, we obtain a bandgap for out-of-plane modes of around 1.9 MHz. Similar to Refs. [6, 45] we remove and displace holes in the center of the PnC to break the symmetry of the lattice and form a defect in the PnC (Fig. 7(c)), to which the mechanical mode of interest is confined, Fig. 7(d). By adjusting the shape



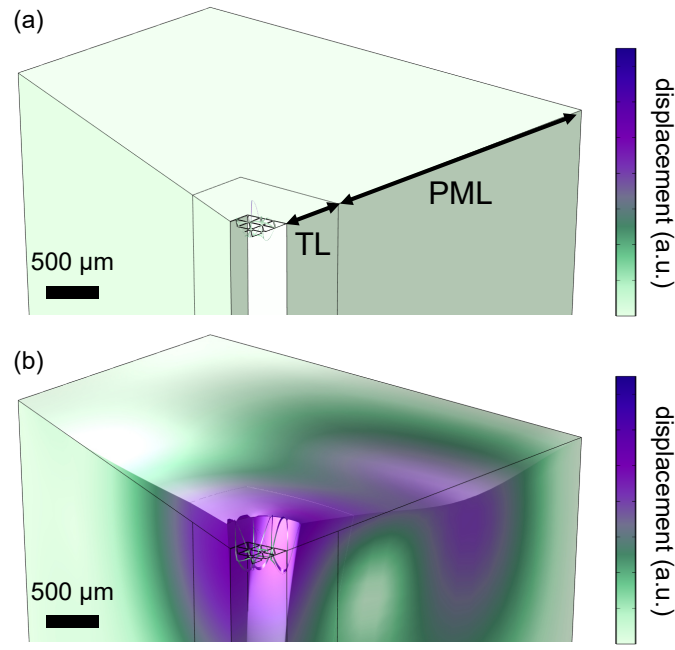


Figure 6. **FEM simulation of mode displacement.** (a) The defect mode and (b) low- $Q_{\text{rad}}$  mode with a perfectly matched layer (PML) and a transition layer (TL).

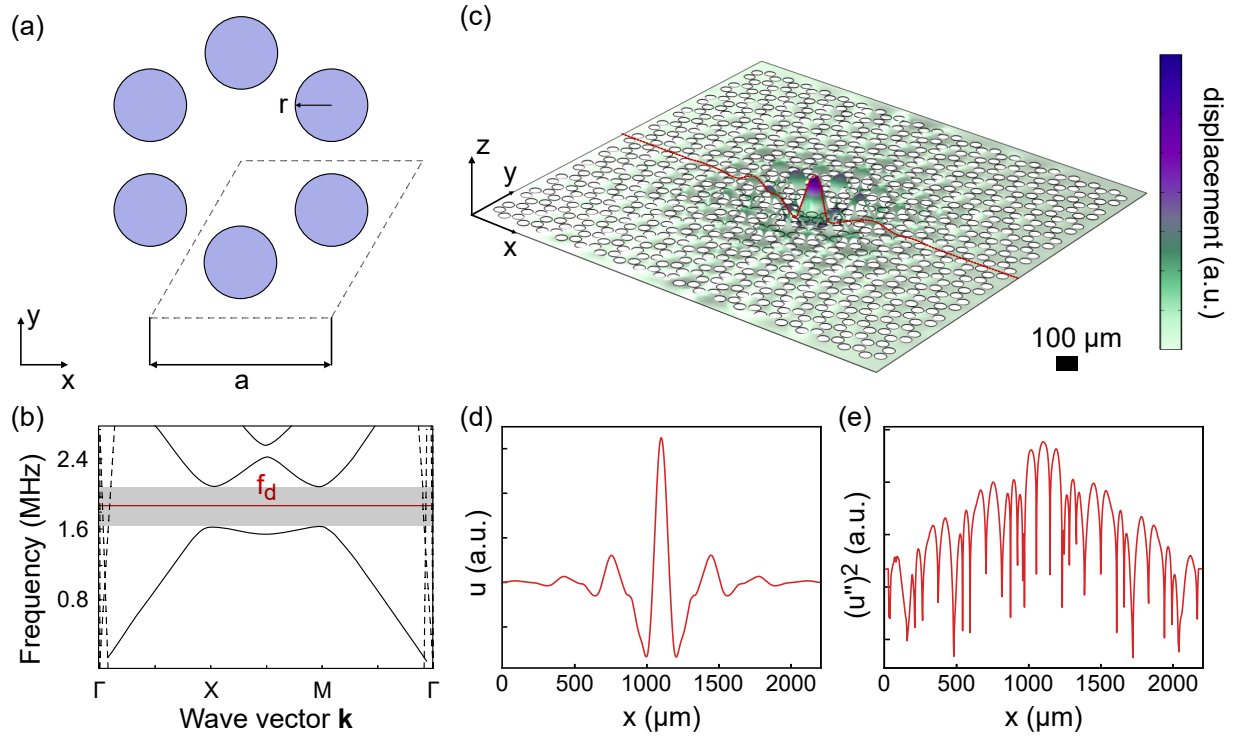


Figure 7. **FEM simulation of a honeycomb membrane PnC with circular holes.** (a) PnC unit cell with circular holes. (b) Phononic band structure of the unit cell. Solid lines are out-of-plane modes and dashed lines are in-plane modes. Grey area highlights the quasi-bandgap. (c) Mechanical displacement of the defect mode in the PnC. (d) The displacement and (e) curvature profiles along the red line marked in (c).

of the defect, we place the mechanical mode at a frequency of 1.87 MHz and obtain a simulated  $Q_m = 7.1 \times 10^6$ . We used 8 unit cells in each direction from the center defect for this PnC geometry.

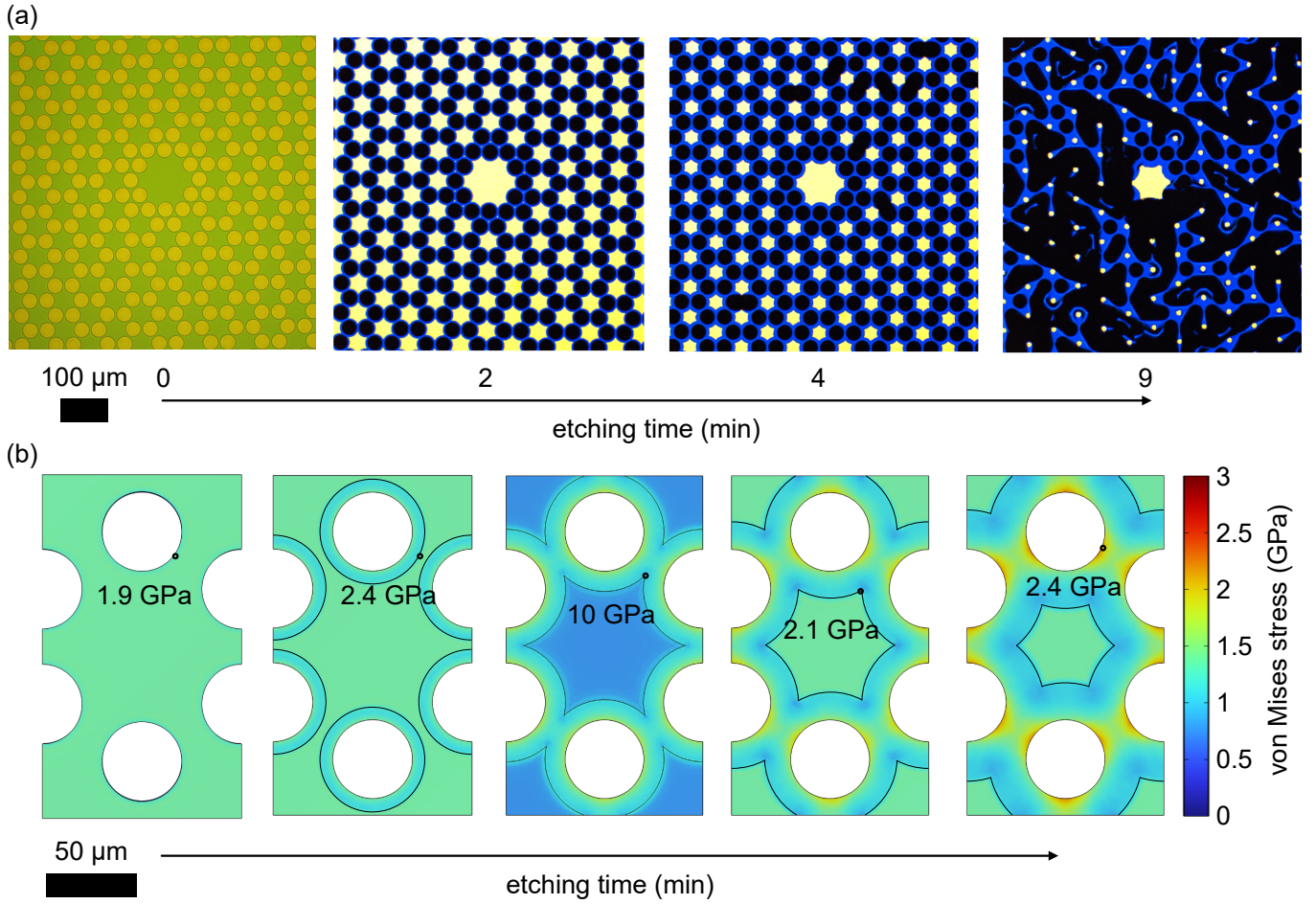


Figure 8. **Release process of the PnC with circular holes.** (a) Optical images of the honeycomb membrane PnC at different etching times. (b) FEM simulations indicating the maximum stress of the structure during the release process in the unit cell ( $a = 110 \mu\text{m}$ ).

When attempting fabrication of the hexagonal PnC with circular holes, it was not possible to release such structure successfully, see Fig. 8(a). To understand the unsuccessful release, we performed FEM simulations of the structure at different times of the fabrication, i.e., at different underetch lengths. Fig. 8(b) shows the stress in the unit cell at different etching times. We observe that at the moment when the tethers are suspended, the formed undercut has a sharp feature that causes the stress in the film to go above 9 GPa. However, the exact value of the stress at the sharp undercut depends on the FEM meshing, which is used in the static solution simulation. Depending on this meshing, the stress can vary between 9 and 20 GPa. We assume that this high value of stress is beyond the yield stress of the AlN film and, thus, leads to cracking and a failed release process.